Seventh International Conference on Computational Fluid Dynamics (ICCFD7), Big Island, Hawaii, July 9-13, 2012

ICCFD7-3102

Towards Hybrid Grid Simulations of the Launch Environment

S. Moini-Yekta[†], M. Barad[*], E. Sozer[‡], J. Housman[*], C. Brehm[‡] and C. Kiris[*]
Corresponding author: shayan.moini-yekta@nasa.gov

[†] University of California Davis, USA.
[‡] Science and Technology Corporation, USA.
[*] NASA Ames Research Center, USA.

Abstract: A hybrid grid approach has been developed for the simulation of next generation heavy-lift space vehicles in the launch environment. The motivation for the hybrid method is to reduce the turn-around time of computational fluid dynamic simulations and improve the ability to handle complex geometry and flow physics. The LAVA (Launch Ascent and Vehicle Aerodynamics) hybrid scheme, consists of two solvers: an off-body immersed-boundary Cartesian solver with block-structured adaptive mesh refinement and a near-body unstructured body-fitted solver which includes conjugate heat transfer. Two-way coupling is achieved through overset connectivity between the off-body and near-body grids. This work seeks to determine the best practices of the individual flow solvers, perform verification with code-to-code comparisons and validation using flight data. Representative unsteady 2D trench and 3D Space Shuttle (STS-135) test cases are used in the analysis.

Keywords: Computational Fluid Dynamics, Immersed-Boundary, Cartesian Methods, Unstructured, Overset, Hybrid Grid Methodologies, Adaptive Mesh Refinement.

1 Introduction

NASA is currently developing a heavy-lift launch vehicle and next generation launch site to carry large payloads for future human exploration missions beyond low Earth orbit. The greater thrust of heavy-lift vehicles requires accurate analysis to ensure vehicle stability, payload safety, and durability of the jet plume impingement region of the launch pad. CFD support is essential in the analysis and design of vehicles and the launch environment. Launch induced pressure and thermal environments have been a concern for NASA for several decades. Historically, analysis relied on experimental and analytical approaches to model plume interaction and design the launch site [1]. High fidelity CFD simulations allow for the rapid and accurate analysis of vehicle and launch site configurations and designs [2]. The simulations provide time-dependent pressure and thermal loading for large-scale trade and comparison studies. With these capabilities, both vehicle and launch site conceptual designs and configurations can be quickly iterated on during design cycles.

The launch environment contains a variety of highly complex geometric details (Figure 1) and flow physics that are challenging to model with traditional CFD methods. Examples of this include: multi-phase reacting flow, unburned particles from engines, interaction of jet plumes with the water sound suppression system and unsteady shock structure development. The focus of this work is to assess the performance of simplified physics models for the pressure and thermal environments. During ignition of the solid rocket boosters (SRB), an ignition overpressure (IOP) wave is generated and travels between the mobile launch platform (MLP), the main flame deflector (MFD) and the vehicle. The IOP wave occurs within the first seconds of launch and may affect the stability of the vehicle. The immersed-boundary Cartesian module of the Launch Ascent and Vehicle Aerodynamics (LAVA) framework, LAVA-Cartesian, is utilized for the

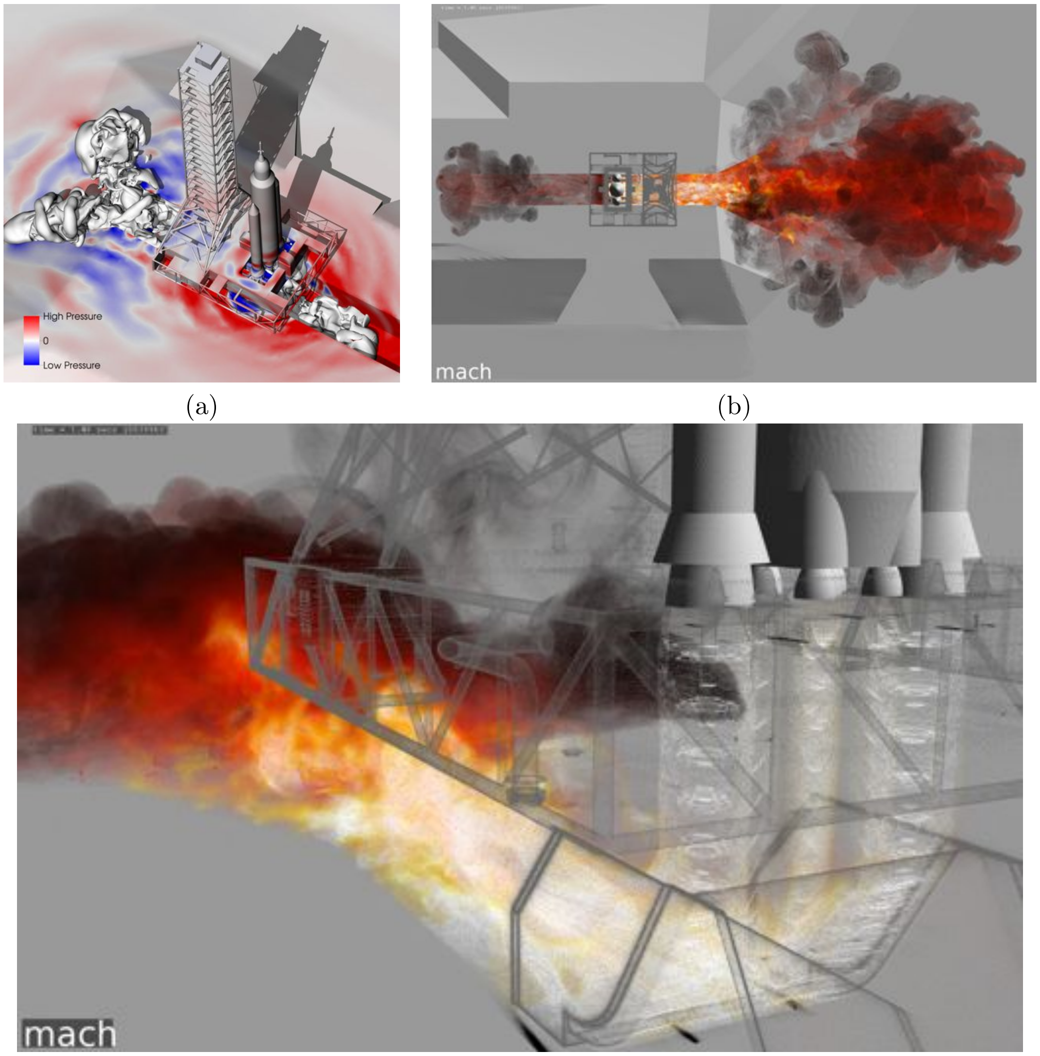

(a) (b) (c)

Figure 1: Examples of CFD simulation of the launch environment: (a) pressure signature and plume isosurface, and particles visualization colored by Mach number ((b) top view and (c) perspective view).

pressure environment. With adaptive mesh refinement (AMR), LAVA-Cartesian has the capability to track and resolve flow features such as pressure waves. This methodology is capable of automatically generating, refining, and coarsening nested Cartesian grids.

Thermal analysis of the launch environment focuses on the main flame deflector, which must withstand the harsh conditions of vehicle launches. Refractory material coating is applied to the MFD to absorb the high temperatures and heat rates to protect against erosion and debris. Boundary layer resolution is critical for the heating and shear prediction for such environments. An unstructured approach is used in order to model complex geometry with viscous wall spacing. An arbitrary polyhedral unstructured solver, LAVA-Unstructured, is used which includes a conjugate heat transfer method for modelling surface heat transfer between the fluid and solid interface. The inclusion of a conjugate heat transfer method enables the properties of the refractory material to be modeled. Fluid-solid thermal interaction is not taken into account with standard adiabatic simulations.

A hybrid LAVA-Cartesian/Unstructured grid approach is motivated by CFD prediction requirements for both the pressure and thermal environments. More specifically, the hybrid approach seeks to reduce CFD simulation turn-around times and improve the ability to handle complex geometries and flow physics.

LAVA-Cartesian/Unstructured seeks to combine the computational efficiency and AMR capabilities of LAVA-Cartesian with the flexibility of body-fitted unstructured grids using LAVA-Unstructured. Unstructured near-body meshes can be used for regions in which viscous resolution is required, while an immersed-boundary Cartesian mesh can be used to track flow features and where wall resolution is not required. To assess the proposed hybrid approach, code-to-code comparisons are done on a 2D trench case and validation is done on a 3D Space Shuttle (STS-135) test case with flight data.

The first section of the paper is an overview of the LAVA framework used for the simulations. Next, the 2D trench benchmark problem is presented. An overview of the problem setup, boundary conditions and simulation procedure is shown. Also, verification is shown via comparisons of unsteady pressure point probes, temperature point probes and general flow field characteristics for different CFD codes. In the subsequent section, the 3D STS-135 validation case is presented. A description of the computational model, experimental point sensor locations and computational grids are included. An in-depth analysis of the pressure and thermal environments are also described. In the last section, a summary of the conclusions and best practices is presented.

2 Numerical Methods

The LAVA framework is a set of project driven codes developed by the authors in the Applied Modeling and Simulation Branch at NASA Ames Research Center. With strict project deadlines, rapidly changing geometries and the unsteady time-dependent simulation requirements, a robust and flexible CFD framework is necessary. Conventional approaches to modeling the launch environment are either structured curvi-linear body-fitted solvers such as OVERFLOW or fully unstructured solvers. OVERFLOW is a well known and validated viscous Reynolds Averaged Navier Stokes (RANS) flow solver using structured overset grids [3]. Despite the advantages of the structured overset methodology, the generation of the structured body-fitted grids and proper grid connectivity require a high level of user-expertise and significant time [4]. Topological changes in geometry require regeneration of grids, despite grid scripting technologies aimed at simplifying and automating the process [5]. Unstructured approaches can be utilized to generate meshes with complex geometry with less user input. However, structured grids are more computationally efficient to store and solve on than unstructured grids. Hybridizing Cartesian and unstructured approaches seeks to balance the benefits of the two.

2.1 LAVA-Cartesian

LAVA-Cartesian is a block-structured immersed-boundary AMR code that is well suited for the launch environment. AMR is a proven methodology for multi-scale problems with an extensive existing mathematical and software knowledge base [6, 7, 8, 9, 10]. The code has been extended using data structures and inter-level operators from the high-performance Chombo AMR library [11] to provide a multi-resolution capability that can coarsen and refine as a simulation progresses (Figure 2a). A sharp immersed-boundary representation [12] and automatic grid generation requiring only a surface triangulation make it possible to easily model complex geometry. The code is a compressible RANS solver with multi-species (no chemical reactions) and unsteady capabilities using dual-time stepping. For stand-alone simulations the inviscid equations are solved due to the cost associated with viscous grid spacing requirements for uniform Cartesian grids.

2.2 LAVA-Unstructured

LAVA-Unstructured is a body-fitted code that utilizes arbitrary polyhedral cells. The code uses a cell-centered finite volume formulation with an unsteady dual-time stepping scheme. With the ability of unstructured grids to resolve viscous and thermal boundary layers, LAVA-Unstructured is well suited for the MFD thermal environment. The compressible RANS equations are solved with the Spalart Allmaras (SA) [13] or Shear Stress Transport (SST) [14] turbulence models. For realistic surface temperature and heat rate prediction, a conjugate heat transfer method is utilized. The conjugate heat transfer method assumes 1D solid thermal conduction with temperature dependent material properties. Fluid-solid thermal coupling is done at the sub-iteration level and solved at each face on the surface. A graphical representation of the conjugate heat transfer method is shown in Figure 2c.

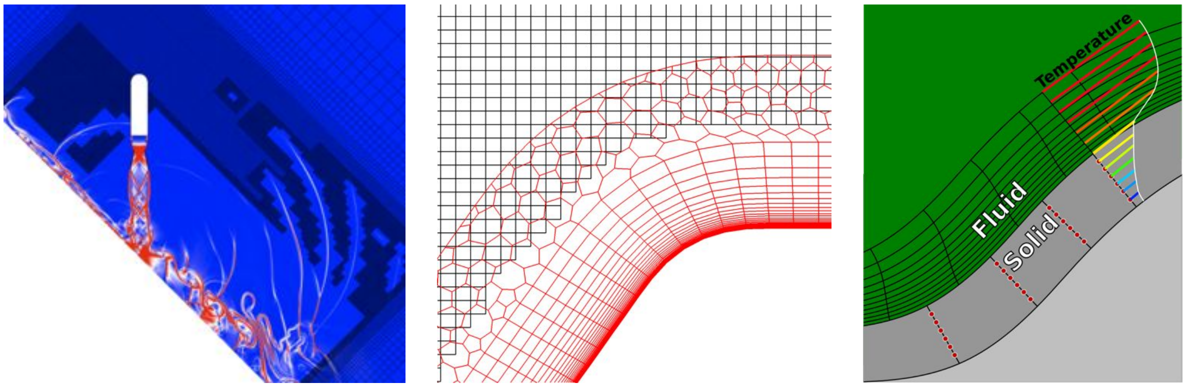

(a) (b) (c)

Figure 2: Highlights of LAVA framework features: (a) block-structured Cartesian AMR feature tracking, (b) hybrid grid coupling of Cartesian and unstructured grids via overset and (c) schematic of conjugate heat transfer method between body-fitted-unstructured and 1D solid grids.

2.3 LAVA-Cartesian/Unstructured

A hybrid block-structured Cartesian/unstructured grid approach with overset connectivity is utilized. Near-body unstructured meshes resolve viscous boundary layers with the LAVA-Unstructured solver. An off-body block-structured Cartesian AMR grid is utilized to efficiently track features with LAVA-Cartesian. The immersed-boundary method is used for regions which do not require viscous spacing (e.g. the tower on the MLP). Communication between the off-body and near-body meshes is achieved with overset connectivity/interpolation. Currently, explicit hole cutting with two layers of fringe points are used. Two-way coupling is done at the sub-iteration level with primitive variables exchanged between the solvers.

3 2D Trench Test Case

A 2D trench test case is used to establish the spatial and modeling requirements of launch environment simulations on a small problem. The performance of different modeling approaches are analyzed by performing inviscid single gas and multiple-species as well as viscous unstructured and hybrid approaches. To assess the different approaches, code-to-code comparisons are done using OVERFLOW and the LAVA framework.

3.1 Problem Setup

To emulate the launch environment, the 2D trench test problem consists of a supersonic jet impinging on a MFD. A simplified MLP is also included in the geometry to incorporate the confinement effect of the exhaust holes. Unsteady pressure conditions are specified at the nozzle exit with a tanh ramping function to mimic engine conditions. The outer domains are set to 200 times the nozzle diameter. For inviscid simulations all surfaces are set to slip boundary conditions, while the viscous simulations set the MFD and a small region around it to no-slip (the red region in Figure 3c). Simulations are done for a total of 2.0 seconds with a time step of 3.5×10^{-5} based on best practices for 3D simulations.

With the 2D setup, the unsteadiness and shock structures are expected to be different but display qualitatively similar behavior as 3D simulations. To monitor the flow, 28 point probes are placed near the plume impingement location. All simulations were run unsteady with dual-time stepping and second-order spatial and temporal discretization. The LAVA codes were run with 30 pseudo-time steps based on best practices and the OVERFLOW simulation was run with 100 based on a sub-iteration study. Both LAVA-Cartesian/Unstructured and OVERFLOW used the Spalart-Allaras RANS turbulence model. An in-depth study of space-time convergence was done by Housman [15] on a similar 2D test case.

3.2 Computational Grids

The generation of the 2D volume grid required several strategies to be implemented. A plume grid spacing of 15 cm was targeted for the plume and main flame deflector region to resolve the flow structure. Additional resolution was placed on the north side of the flame trench to track flow features. The Cartesian mesh is shown in Figure 3a and uses a seven level AMR grid with approximately 850k cells. Refinement boxes were specified around the nozzle, plume region and MFD and are easy to identify in the image. The unstructured grid emulates the Cartesian mesh but is coarsened away from the MFD to reduce the cell count. Figure 3b shows the prismatic/polyhedral mesh which features viscous spacing (2.0×10^{-6} wall spacing for a $y^+ \approx 1$) on the MFD and 292k cells.

The hybrid grid seeks to combine the unstructured viscous wall spacing on the MFD with the efficient AMR off-body of block-structured grids. Hence, a viscous unstructured prismatic/polyhedral grid is specified within a 1 meter region of the MFD surface with a block-structured Cartesian off-body mesh and immersed-boundary treatment on the other surfaces. The grid is shown in Figure 3c and contains 397k Cartesian cells and 30k unstructured cells. The OVERFLOW grid is also shown in Figure 3d and contains 640k grid points with 321 grid zones. Viscous spacing is also specified on the MFD with similar resolution in the plume and trench.

3.3 Results

To determine the performance of the different fidelity approaches, several aspects were analyzed for this test problem. The first aspect is the performance of single gas and multi-species simulations for the pressure environment. Simulations are completed using LAVA-Cartesian with inviscid single gas and multi-species models. The unsteady pressure history is shown in Figure 4 for point probes 2, 7 and 17. These points were selected to analyze the pressure history inside the jet plume, near the first impingement location and near the termination of the Mach diamond at the bottom of the deflector. The single gas and multi-species pressure histories show good correlation at all three points. The IOP magnitude is well predicted between the approaches for all locations as well. Similar trends are observed for the single gas and multi-species results, however a small phase shift is evident due to the differences in wave propagation speed.

A second modeling option that is considered is inviscid vs. viscous discretizations. A comparison of the instantaneous Mach number distributions at t=0.4s for the LAVA-Cartesian multi-species, LAVA-Unstructured, LAVA-Cartesian/Unstructured and OVERFLOW simulations are shown in Figure 5. The flow structure is similar between the four simulations with the plume primarily deflected to the north side (shown to the left on the images) of the trench and shock structures near the step of the deflector. The higher resolution of the LAVA-Cartesian and OVERFLOW simulations is evident by the finer flow structures in the trench. The hybrid LAVA-Cartesian/Unstructured simulation compares well with the individual solvers and OVERFLOW, which is encouraging. Note the plume expansion rate appears wider due to the coarser resolution for LAVA-Unstructured while all the viscous simulations are wider than the inviscid simulation partially due to turbulent mixing in the shear layer.

To assess the performance of the hybrid approach, the unsteady pressure probes were compared between LAVA-Cartesian/Unstructured and OVERFLOW. Three points were selected again: inside the plume (point 2), near the first impingement (point 18) and near the recirculation region at the bottom of the MFD (point 9). The unsteady pressure is shown in Figure 6 for the two approaches. Higher frequency oscillations are present in the OVERFLOW solution due to the higher grid resolution in comparison to LAVA-Cartesian/Unstructured. Inside the plume, the pressure history shows excellent comparison. Close to the wall the unstructured near-body grid resolves the boundary layer development for LAVA-Cartesian/Unstructured and is in agreement with OVERFLOW. The IOP magnitudes and trends compare well between the two codes.

With the viscous simulations, accurate temperature prediction is also important. Figure 7 shows the unsteady temperature history for point probes 2, 9 and 18 for LAVA-Cartesian/Unstructured and OVERFLOW. In the plume, a higher initial temperature peak is evident in OVERFLOW which can also be associated with the higher grid resolution. Following the peak, a similar trend is clear between the two solvers. Closer to the MFD, at point 9 and 18, similar trends can be observed between the solvers. Overall a good comparison is seen between the hybrid LAVA-Cartesian/Unstructured and OVERFLOW simulations. Additional simulations will be conducted with better matching grid resolutions to investigate the higher frequency discrepancies.

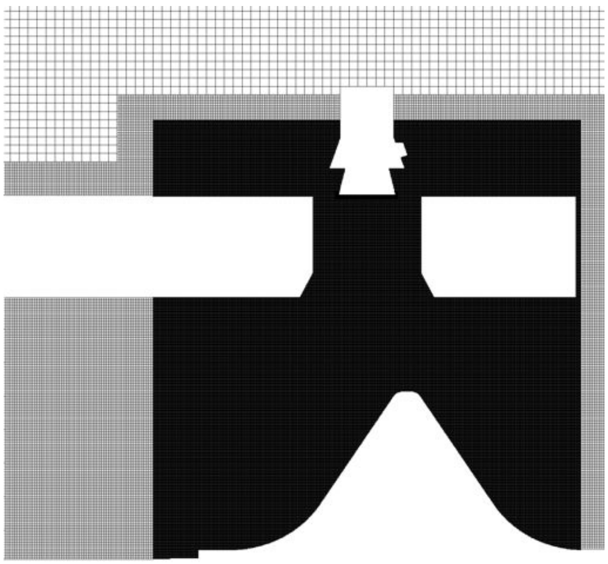

(a) LAVA-Cartesian

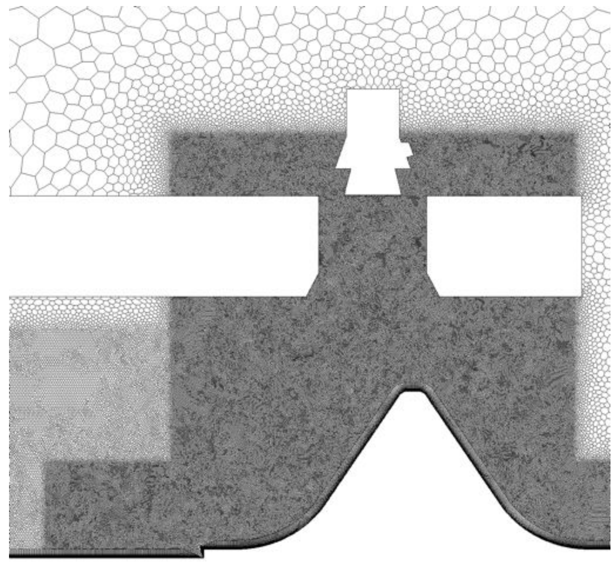

(b) LAVA-Unstructured

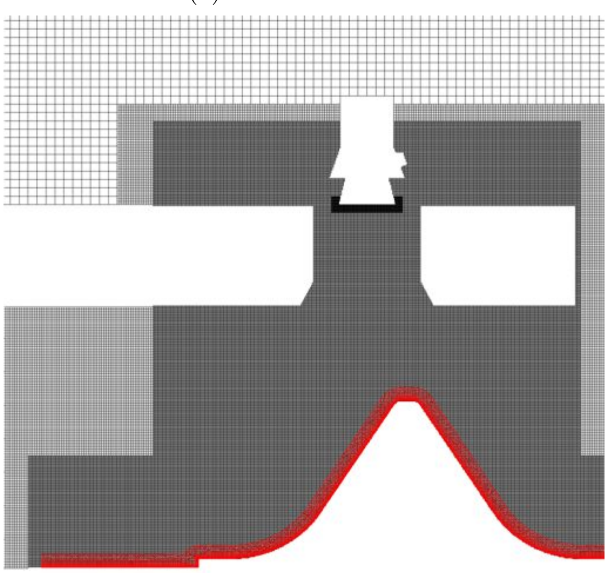

(c) LAVA-Cartesian/Unstructured

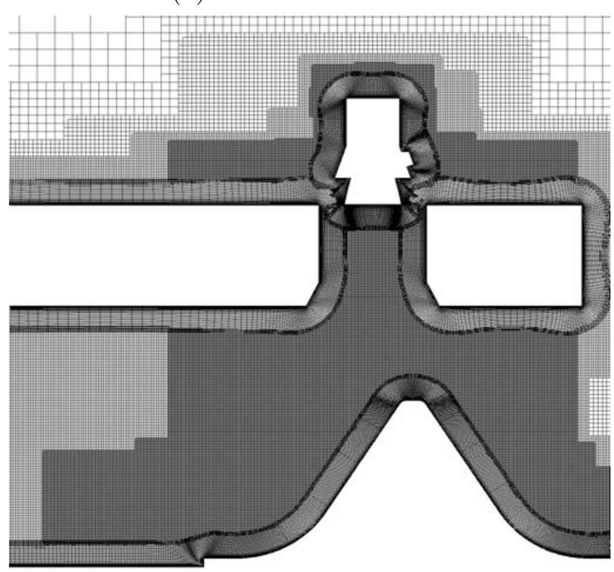

(d) OVERFLOW

Figure 3: Computational grid for 2D trench test case for (a) LAVA-Cartesian, (b) LAVA-Unstructured, (c) LAVA-Cartesian/Unstructured (unstructured shown in red) and (d) OVERFLOW.

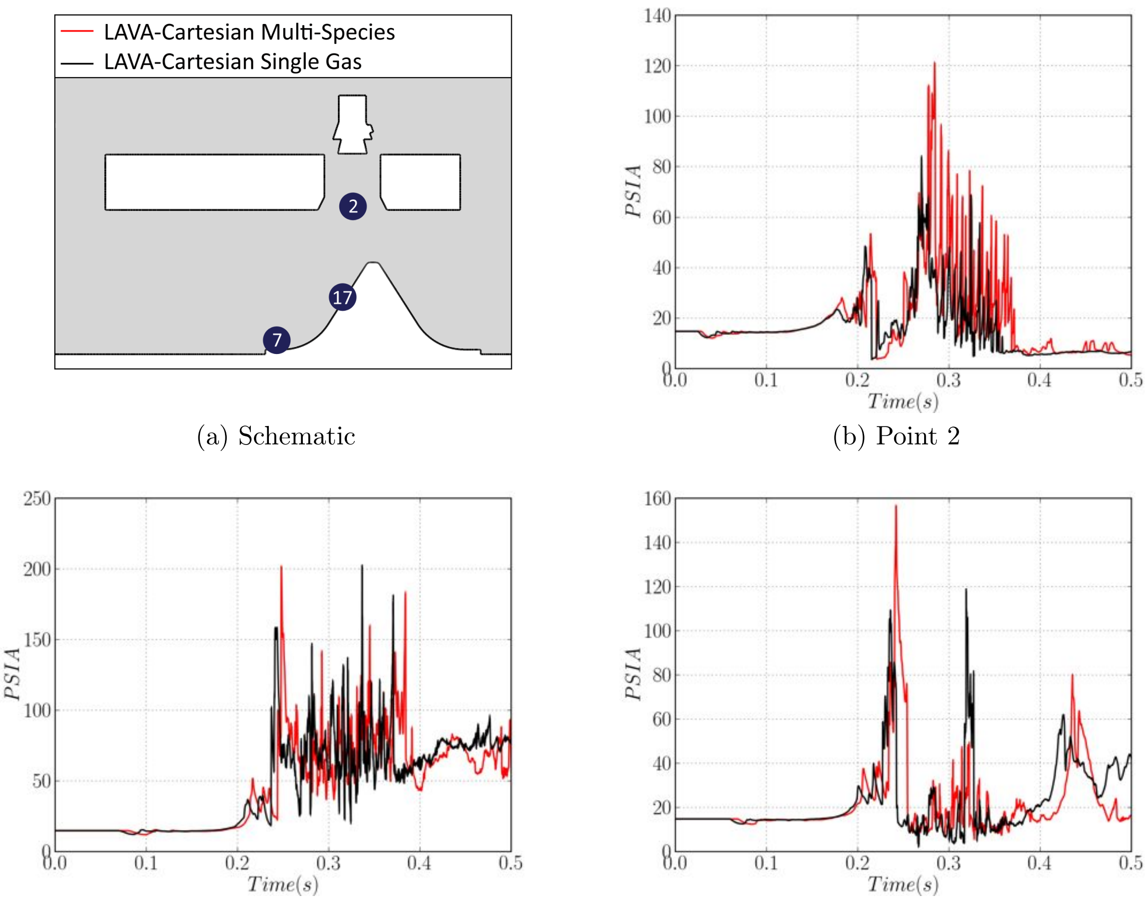

(a) Schematic

(b) Point 2

(c) Point 7

(d) Point 17

Figure 4: Unsteady point probe pressure history: (a) schematic of the point sample locations, at (b) point 2, (c) point 7 and (d) point 17 for LAVA-Cartesian inviscid single gas and multi-species.

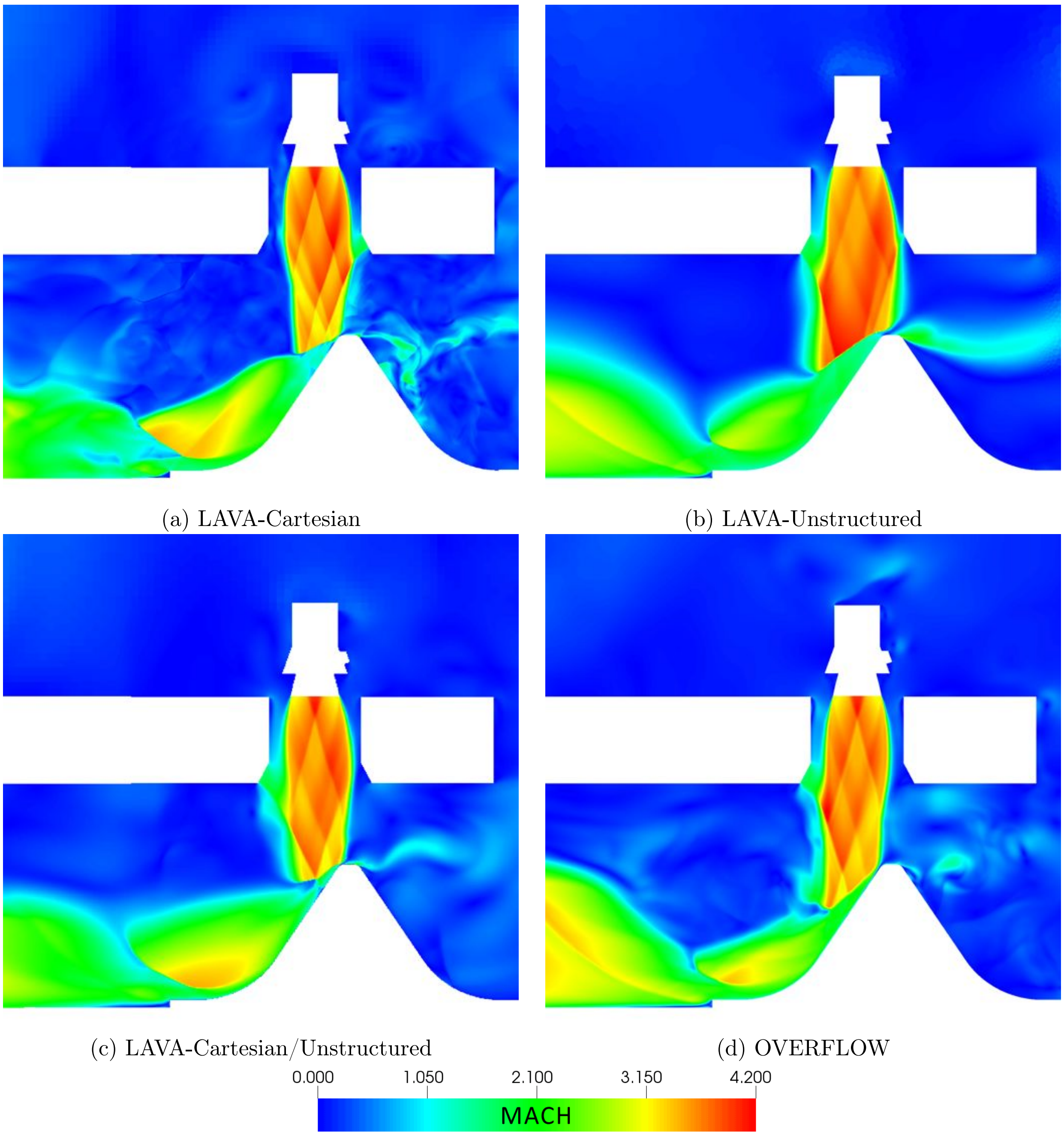

(a) LAVA-Cartesian

(b) LAVA-Unstructured

(c) LAVA-Cartesian/Unstructured

(d) OVERFLOW

Figure 5: Mach distributions at t=0.4s for 2D trench test case using (a) LAVA-Cartesian, (b) LAVA-Unstructured, (c) LAVA-Cartesian/Unstructured and (d) OVERFLOW.

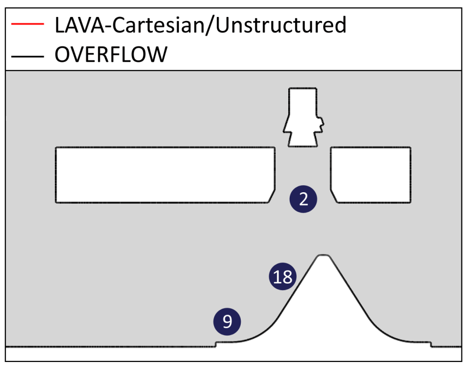

(a) Schematic

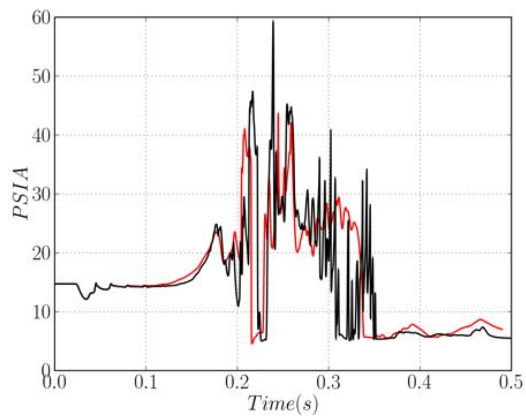

(b) Point 2

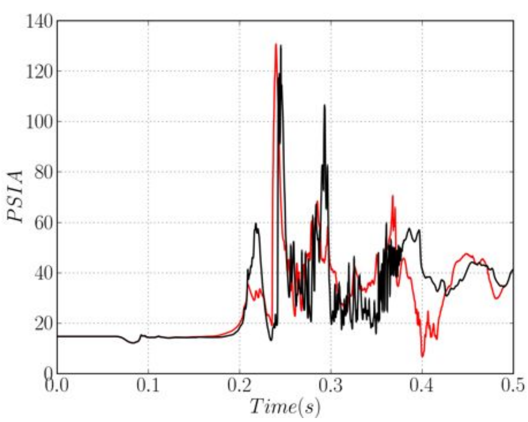

(c) Point 9

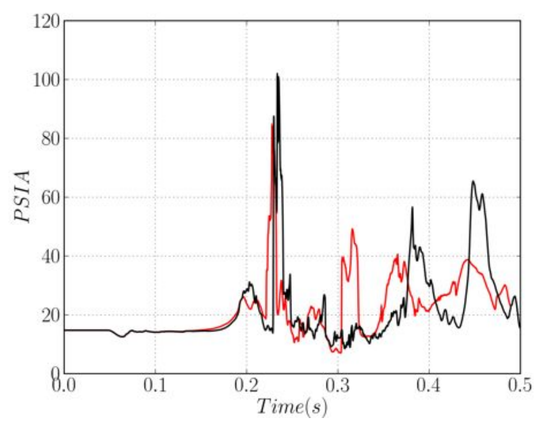

(d) Point 18

Figure 6: Unsteady point probe pressure history: (a) schematic of the point sample locations, at (b) point 2, (c) point 9 and (d) point 18 for LAVA-Cartesian/Unstructured and OVERFLOW.

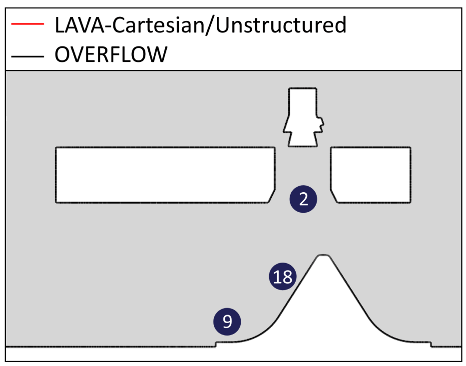

(a) Schematic

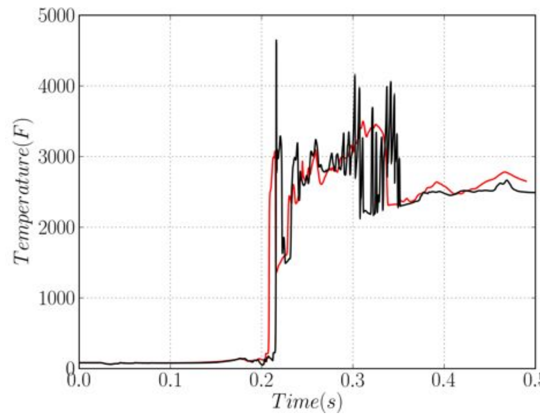

(b) Point 2

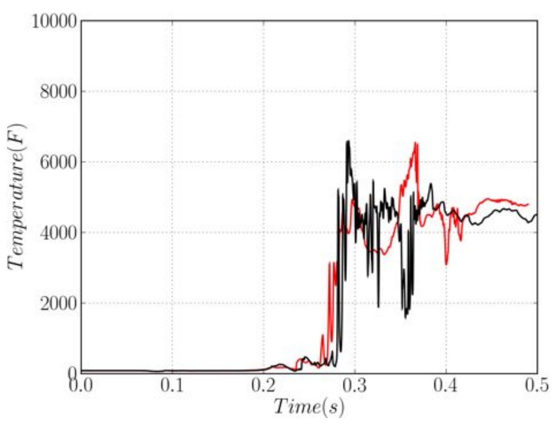

(c) Point 9

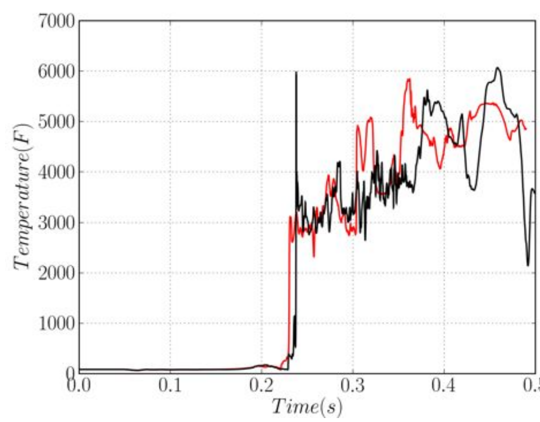

(d) Point 18

Figure 7: Unsteady point probe temperature history: (a) schematic of the point sample locations, at (b) point 2, (c) point 9 and (d) point 18 for LAVA-Cartesian/Unstructured and OVERFLOW.

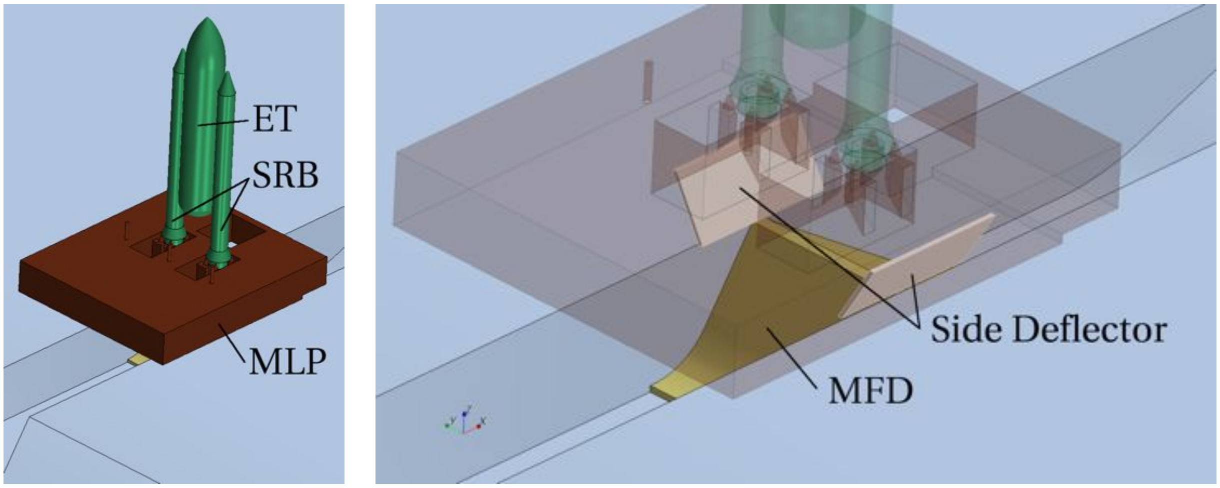

Figure 8: Overview of the computational setup for the STS-135 validation case.

4 Space Shuttle Validation Case (STS-135)

4.1 Problem Setup

The computational geometry for the STS-135 validation test includes the flame trench, surrounding ground terrain, MLP, side deflectors and the launch vehicle. Figure 8 shows an overall schematic of the STS-135 geometry. The flame trench is designed to divert the jet plume and potential debris away from the vehicle. The main component of the flame trench is the MFD located underneath the vehicle nozzles. A simplified vehicle consisting of the external tank (ET) and two SRBs are used in the simulations. The main focus of this work is the induced environment near the MFD, hence a simplified setup is used which excludes the tower and orbiter.

A physical time step of 3.5×10^{-5} seconds with 30 sub-iterations are chosen based on previous experience. The test case is modeled up to 1.4 seconds to capture the IOP wave and plume development. During the simulation time the vehicle is assumed to be static (the actual vehicle moves only a few feet in that time) and the water sound suppression system is not modeled due to complexity. Unsteady boundary conditions are applied at the nozzle exits using the data from the STS-1 launch. The STS-1 boundary conditions have similar conditions as the STS-135, which were not available at the time of this work. Viscous LAVA-Unstructured simulations were completed with the SST turbulence model.

A conjugate heat transfer method was used on the MFD for LAVA-Unstructured. A six inch thick Fondu Fyre coating was assumed on the MFD to emulate the STS-135 launch conditions. Surface temperatures were capped at the melting temperature of the material which is approximately 2000 degrees Fahrenheit. The individual solvers LAVA-Cartesian and LAVA-Unstructured were applied to this problem for validation. Future work will include the application of the hybrid LAVA-Cartesian/Unstructured solver.

4.2 Flight Data

As a part of an investigation of the refractory material coating on the MFD the north side of the MFD was instrumented to record pressure, temperature, acceleration and heat rates. Flight data from the commercial-off-the-shelf (COTS) sensors for the STS-135 launch was used for validation [16]. The sensor locations are illustrated in Figure 9 on the north side of the MFD. The COTS sensors feature Kulite pressure transducers, medtherms and erodible Nanmac thermocouples. The sensor data was filtered using a low pass filter at 50 Hz.

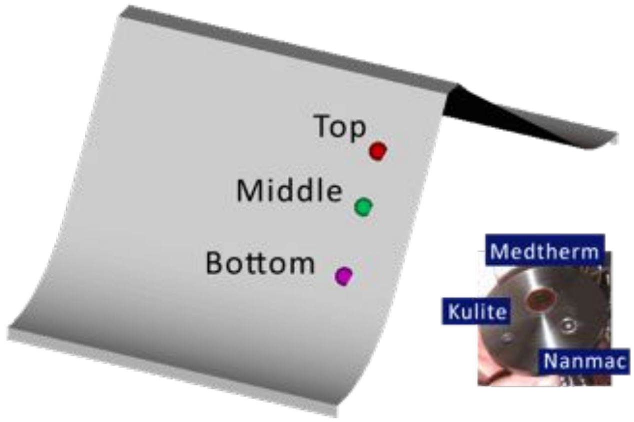

Figure 9: Experimental instrumentation points for north side of main deflector and an image of COTS sensor configuration for STS-135 launch.

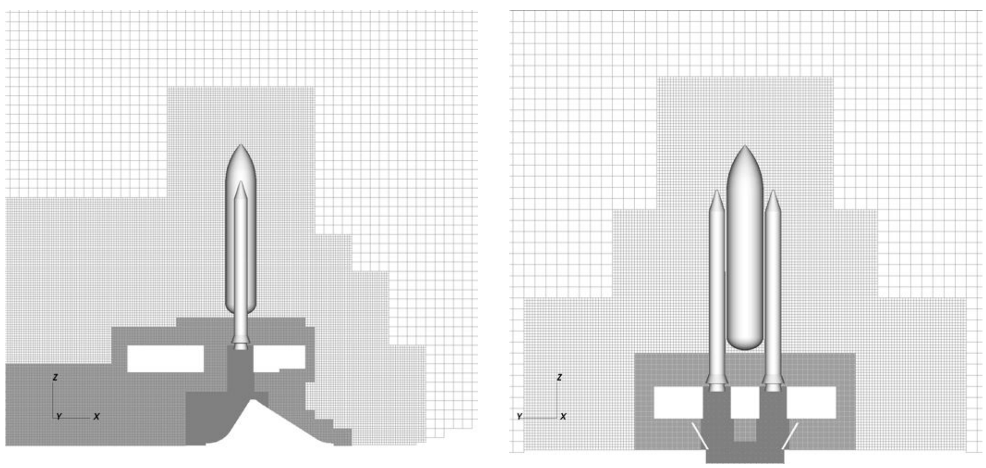

Figure 10: Side views of block-structured immersed-boundary Cartesian volume grid for STS-135 test case.

4.3 Computational Grids

Using the LAVA framework, structured and unstructured computational grids were generated for the STS-135 geometry.

4.3.1 Block-Structured Cartesian Grid

Cartesian mesh generation for LAVA-Cartesian requires only a closed water-tight triangulation as input and automatically produces an immersed-boundary Cartesian mesh. User input can be used to customize the local refinement through either solution gradients, entropy adjoint or geometric features (e.g. component tagging, edge tagging and regions of interest) for a high degree of control. To fully resolve the plume impingement on the MFD, a seven level Cartesian grid was generated. The finest level has a spacing of 3.9 cm to accurately capture the unsteady boundary conditions at the nozzle exits. Regions of interest are used to cluster points underneath the nozzle and in the vicinity of the MFD. The grid is illustrated in Figure 10 along x=0 and y=0 slices. Domain boundaries are set to approximately 450 meters in each direction to avoid reflections off the outer boundaries. The grid consists of 76 million cells in the full domain.

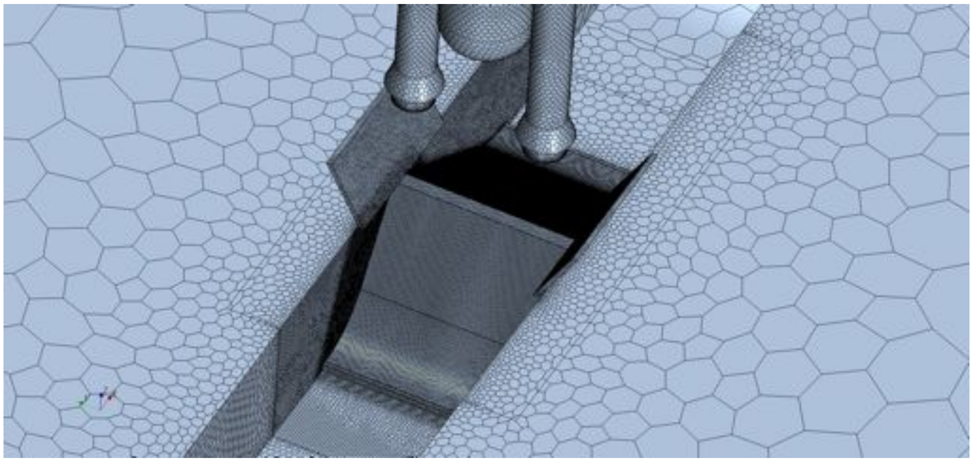

Figure 11: Polygon surface mesh for unstructured grid with MLP hidden for STS.

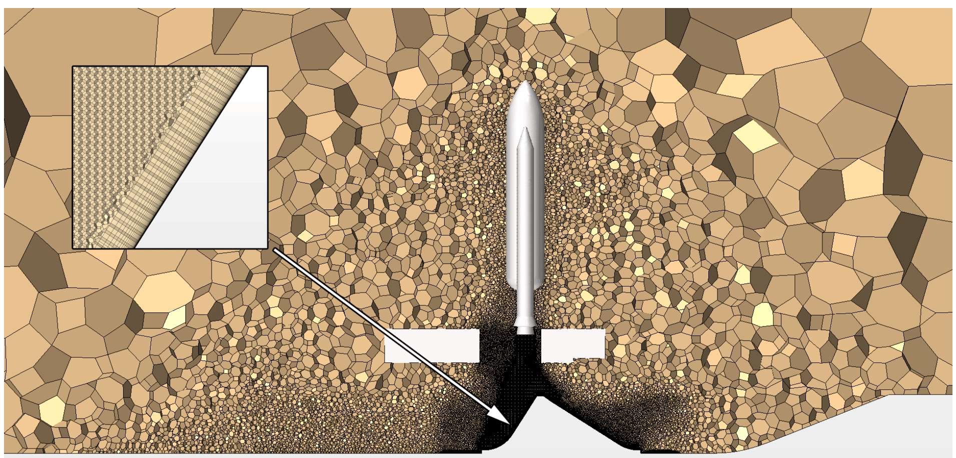

Figure 12: Side view of unstructured prismatic/polyhedral volume grid for STS-135 test case.

4.3.2 Unstructured Grid

The commercial software, STARCCM+ [17], was used to generate the unstructured grid from the surface triangulations. The quality of the unstructured grid is highly dependant on the surface grid, which dictates the resolution of the volume mesh. With the main focus on the trench and plume impingement, higher resolution is applied on the MFD and plume region. A spacing of 0.15 m is applied on the MFD and inside the MLP exhaust holes. Figure 11 shows the surface mesh with the MLP hidden.

Prismatic boundary layer grids were used near the regions of interest (MFD) and a polyhedral mesh was used to fill the remaining domain. Special care was taken to maintain high fidelity in the plume region. The grid is designed to become coarse in the farfield to avoid reflections at the boundaries. A volume specification is used to maintain an edge length of approximately 0.15 m in the plume impingement region. Additional refinement is placed near the nozzle exits to accurately resolve the unsteady boundary conditions. The prismatic grid has a wall spacing of 2.0×10^{-6} and has approximately 57 layers with a stretching ratio of 1.2 to smoothly interface with the polyhedral mesh. These grid parameters follow from the best practices of the 2D trench problem. The grid consists of 6.12 million cells and 1.29 million faces (Figure 12).

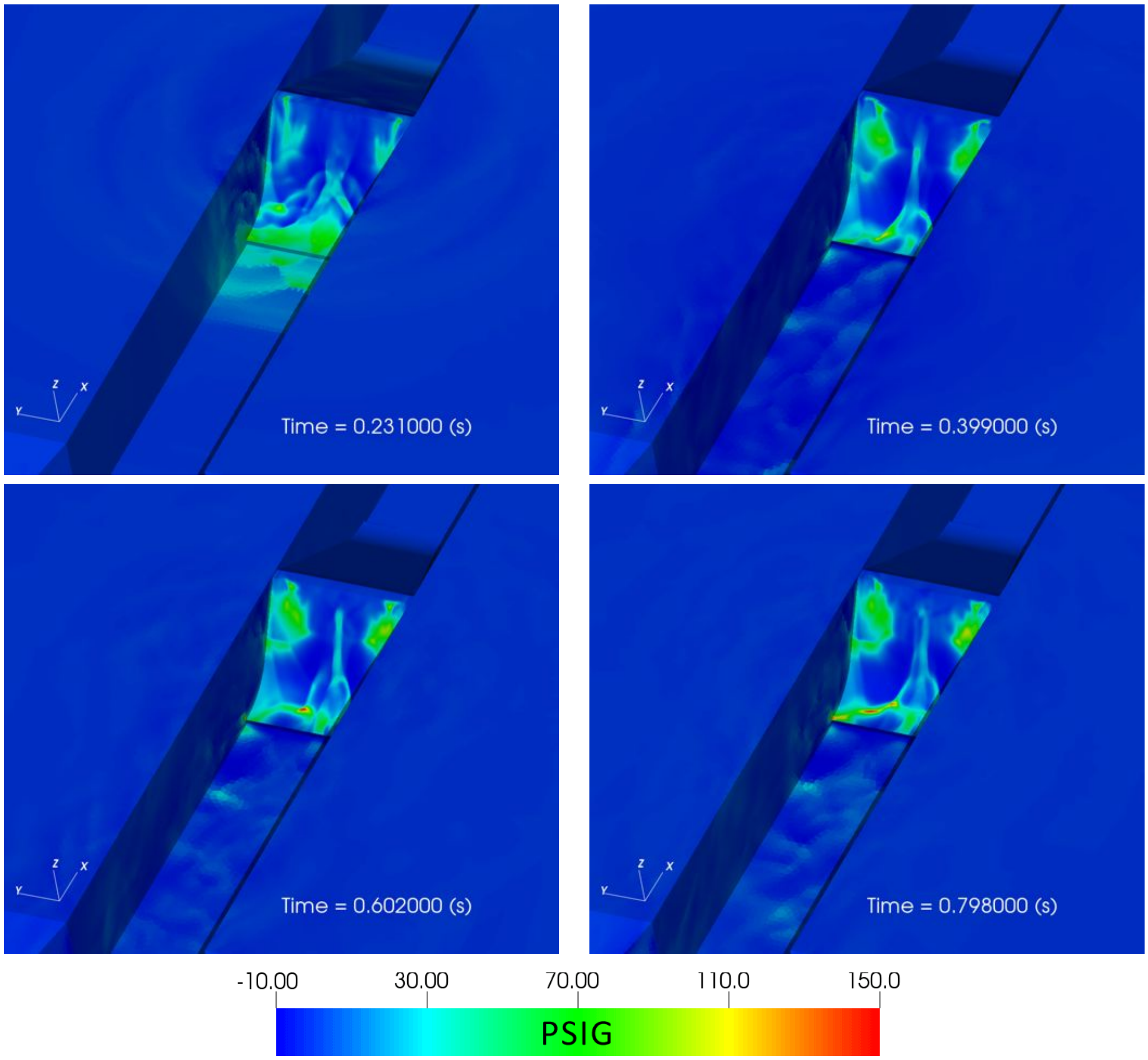

Figure 13: Instantaneous pressure distribution (PSIG) at several times using LAVA-Cartesian

4.4 Results: Pressure Environment

With the unsteady ignition of the SRBs, a large ignition over pressure is generated followed by the impingement of the plume on the MFD. Throughout the development of the flow, multiple shocks are generated on the MFD as the supersonic flow is deflected. This leads to multiple regions of high pressure (impingement points) and low pressure (recirculation points) as the plume develops. To visualize the behavior of this flow field, the gauge pressure distribution (PSIG) is plotted on the surface of the trench in Figure 13 from the LAVA-Cartesian simulation. The time steps are chosen such that the first image illustrates the initial impingement of the plume, flow passing the north side step in the MFD, partially developed flow and in the last image the quasi-steady full thrust conditions. In the initial flow field, the ignition of the SRBs impacts the MFD and disperses along the trench. As the flow develops a distinct shock structure is generated at the curved region of the MFD. Furthermore, with both SRB plumes deflected to the north side of the trench the flow is contained between the trench walls and the opposing SRB plumes.

To visualize the complexity and unsteadiness of the flow field the mass fractions from multi-species LAVA-Cartesian results are shown in Figure 14. Three levels are shown: 95, 50 and 25 percent exhaust gas mass fractions. The 95 percent exhaust gas mass fraction is an indicator of where the majority of the exhaust gas is directed. At the later time sequences, the shear layer instabilities and energetic flow leads to mixing

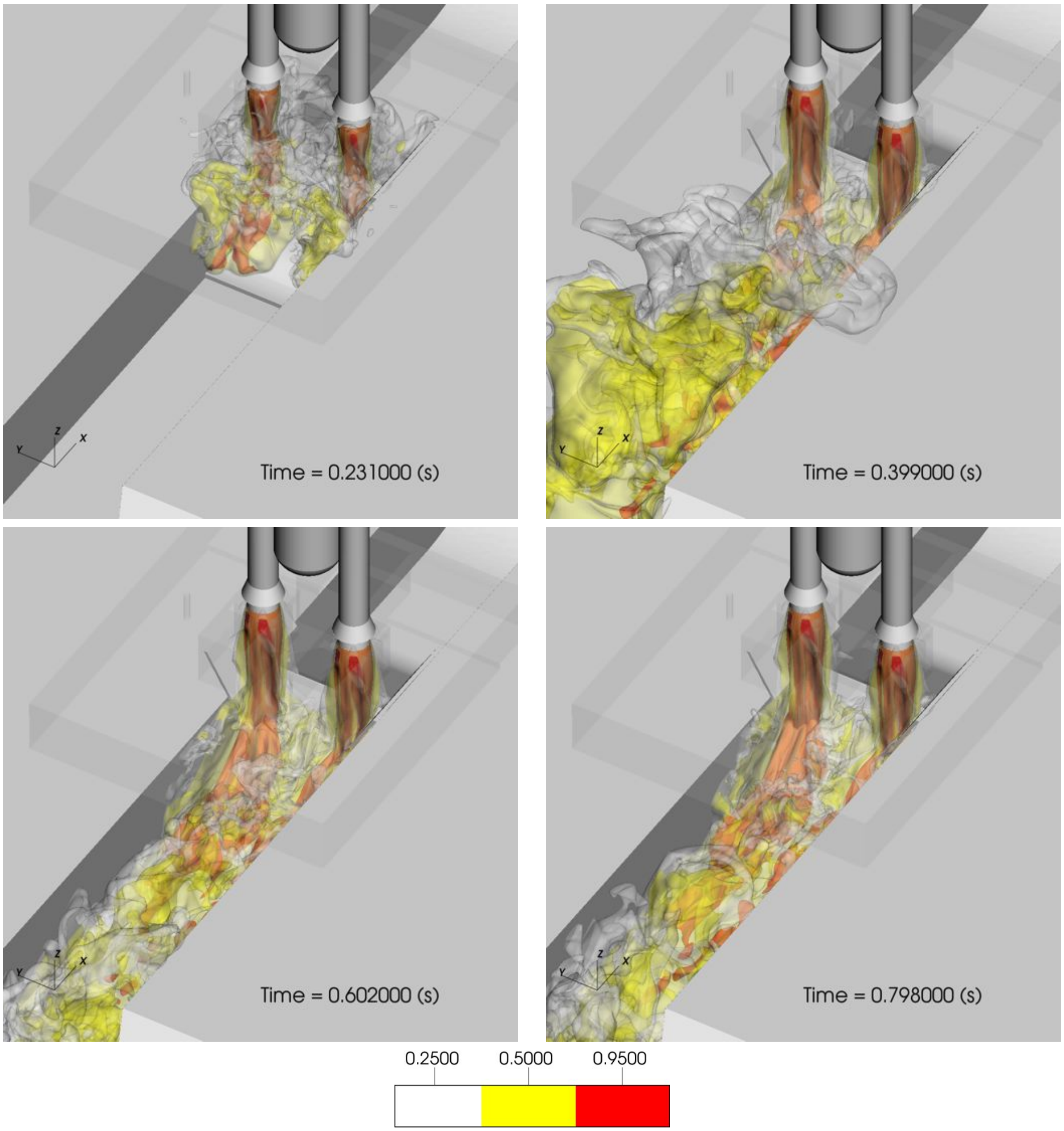

Figure 14: Isosurfaces of exhaust mass fraction at several time sequences using LAVA-Cartesian. Red indicates 95% exhaust gas, yellow is 50% and white is 25%. For better visibility the MLP is shown as transparent.

and reduced concentrations of pure exhaust gas. These plots are also indicators of plume containment of the trench side walls and MFD. The results indicate the plume is well contained inside the trench and becomes highly unsteady away from the MFD.

The interaction of the two plumes with the MFD and trench leads to a complex and unsteady pressure environment. A key aspect of this work is to investigate the required fidelity to accurately predict the pressure environment of this flow field. The LAVA-Cartesian results are obtained by solving the inviscid Euler equations due to the computational advantages of the approach. Inviscid physics dominate the flow, due to the fact that within the nozzle and along the body the boundary layers are generally thin [18]. Also the large density gradients in the flow field lead to shear layer instabilities and growth of Kelvin-Helmholtz

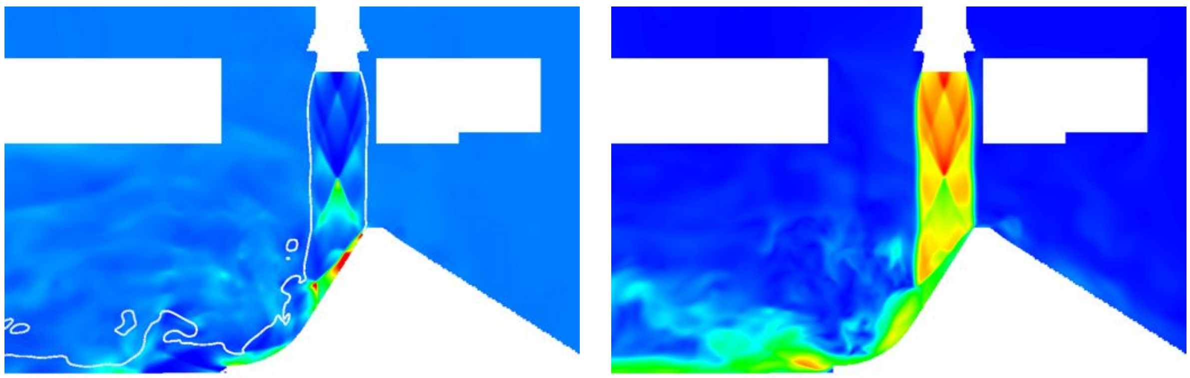

(a) LAVA-Cartesian Multi-Species

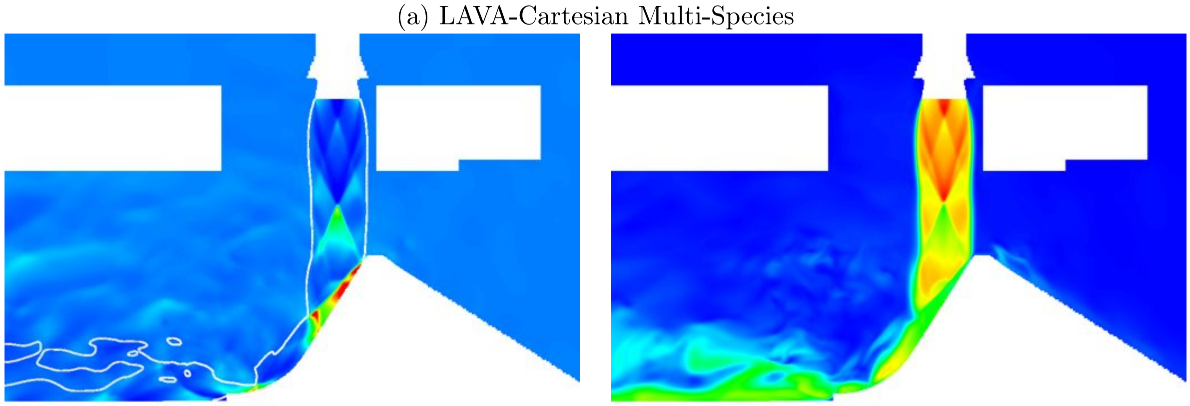

(b) LAVA-Cartesian Single Gas

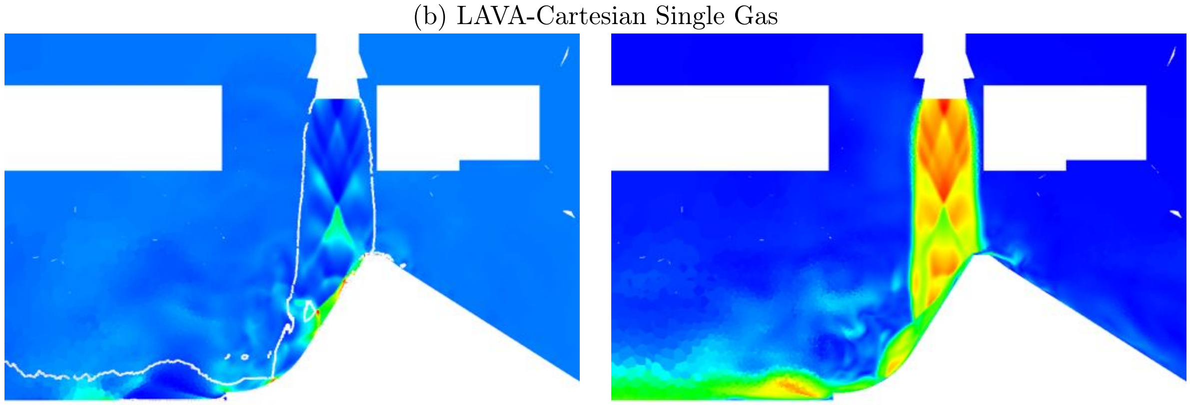

(c) LAVA-Unstructured Viscous Single Gas

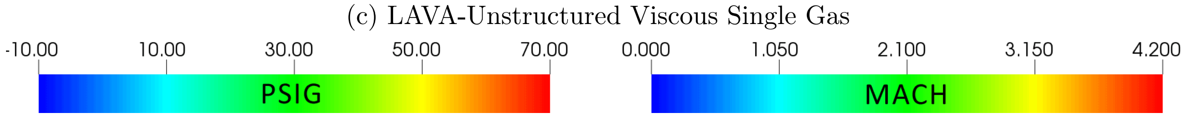

Figure 15: Gauge pressure distributions (PSIG) with white sonic-line contours are shown in the left column with Mach number distributions on the right column at the quasi-steady state full thrust time of t=0.7 seconds. From the top to the bottom: (a) inviscid multi-species, (b) inviscid single gas and (c) viscous single gas.

instability characteristics to the jets [19] which we modelled with the SST turbulence model in the LAVA-Unstructured code. To illustrate this, the pressure and Mach number distributions are shown in Figure 15 for LAVA-Cartesian multiple species and single gas as well as single gas LAVA-Unstructured simulations.

The results are taken at the quasi-steady state full thrust conditions (t=0.7 seconds) with the contour levels of the Mach number set from 0 to 4.2 and the pressure contour range from -10 to 70 PSIG. Sonic lines are

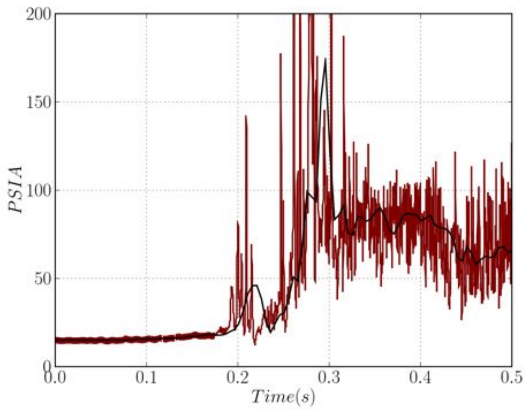

(a) Flight Data

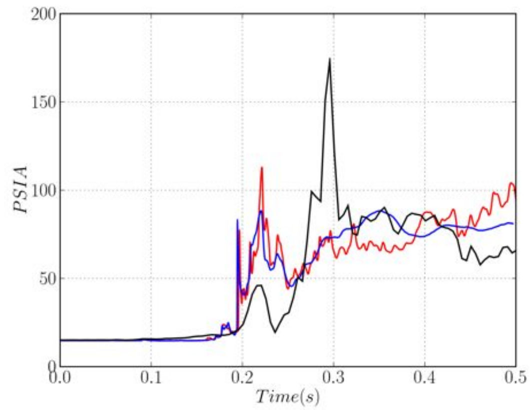

(b) Simulation Data

Figure 16: Unsteady pressure history at top sensor location on MFD. Raw flight data (maroon –), filtered flight data (black –), LAVA-Unstructured viscous (blue –) and LAVA-Cartesian inviscid (red –) are shown.

also shown in the PSIG distribution plots to visualize the shock structure on the MFD. The first observation of the results is that the major structures are consistent between each modeling fidelity level. Mach cones within the jet are sharply defined and the strong shock at the first impingement point are captured. Aside from the higher jet spreading rate, partially due to turbulent mixing, the viscous and inviscid results are consistent. Similarly, the single gas and multi-species results have nearly identical pressure values and shock structures. The results indicate single gas inviscid simulations are sufficient in capturing the MFD pressure environment for these flow fields.

For a quantitative comparison, unsteady pressure probe data was accumulated for the simulation data and flight data. As shown in Figure 9, three locations (bottom, middle and top) were examined on the MFD. Figure 16 shows the unsteady pressure history for the inviscid multi-species, viscous single-species and both the raw and filtered flight data. Comparison of the simulation data to the flight data at the top sensor reveals an approximately 0.1 second phase lag. The source of the phase lag can be primarily attributed to neglecting the multi-phase effects of the water sound suppression system which would slow the plume propagation speed. Another potential cause of the time lag is differences in the ramping of the STS-1 and STS-135 engine conditions. Small discrepancies in the unsteady pressure ramping has the potential to change the plume characteristics. The numerical simulations also do not account for the multi-phase flow and the fact that waves propagate at different speeds in different mediums. However, the more important aspect of the comparison is the pressure peaks and the data trends. On those fronts, the simulation data shows good agreement in capturing the initial IOP and reduction in pressure. Good agreement is also evident between the inviscid and viscous simulation results, consistent with the previous pressure and Mach results. Note, the unfiltered pressure sensor flight data contains high frequency content that is eliminated with filtering.

Similar behavior is observed at the middle and bottom sensor location shown in Figure 17 and 18 respectively. Here the different numerical simulations are in good agreement with each other and capture the IOP and pressure signatures. The median value of the flight data appears to be slightly lower, which again can be attributed to the water sound suppression system dampening the pressure field. The unfiltered pressure sensor flight data exhibits a similar IOP pressure amplitude as the simulation data, which is not true of the filtered flight data.

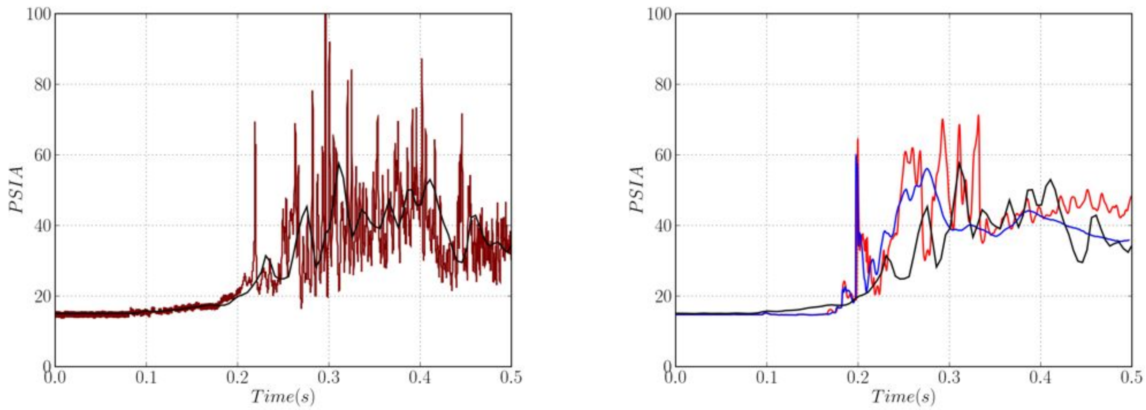

(a) Flight Data (b) Simulation Data

Figure 17: Unsteady pressure history at middle sensor location on MFD. Raw flight data (maroon –), filtered flight data (black –), LAVA-Unstructured viscous (blue –) and LAVA-Cartesian inviscid (red –) are shown.

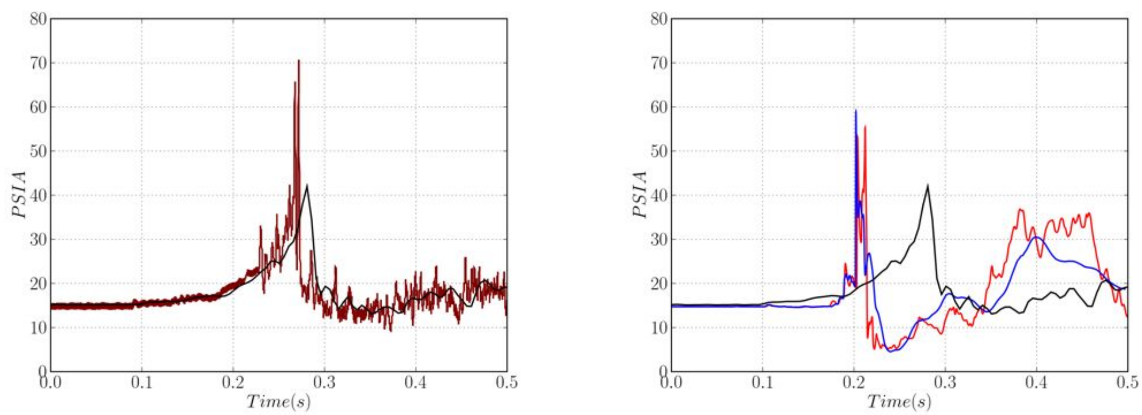

(a) Flight Data (b) Simulation Data

Figure 18: Unsteady pressure history at bottom sensor location on MFD. Raw flight data (maroon –), filtered flight data (black –), LAVA-Unstructured viscous (blue –) and LAVA-Cartesian inviscid (red –) are shown.

4.5 Results: Thermal Environment

The thermal environment plays a critical role in the safety and design of the launch site. In particular, thermal protection on the MFD is designed to withstand the high pressure and temperatures of the impinging jet for multiple launches. Insufficient thermal protection can lead to damage of the trench and the potential for debris which may harm the vehicle. Unlike the pressure environment, where inviscid features dominate the flow, viscous simulations are required to accurately capture the viscous heating at the wall. The proposed approach is to use the viscous turbulent capabilities of LAVA-Unstructured with a conjugate heat transfer methodology to approximate wall heating effects. To visualize the thermal environment, the temperature distribution is shown on the MFD in Figure 19.

Comparison of the temperature and heat rate distributions with the pressure distributions (Figure 13) shows the correlation between high pressure and temperature regions. Near the first impingement point (top sensor) the surface temperature reaches a local maximum. A strong shock develops on the curved region of the MFD leading to a second impingement point. Along the shock, the temperature field indicates a higher temperature and heat rate region. The point sensors are also superimposed on the plot to give a sense of the

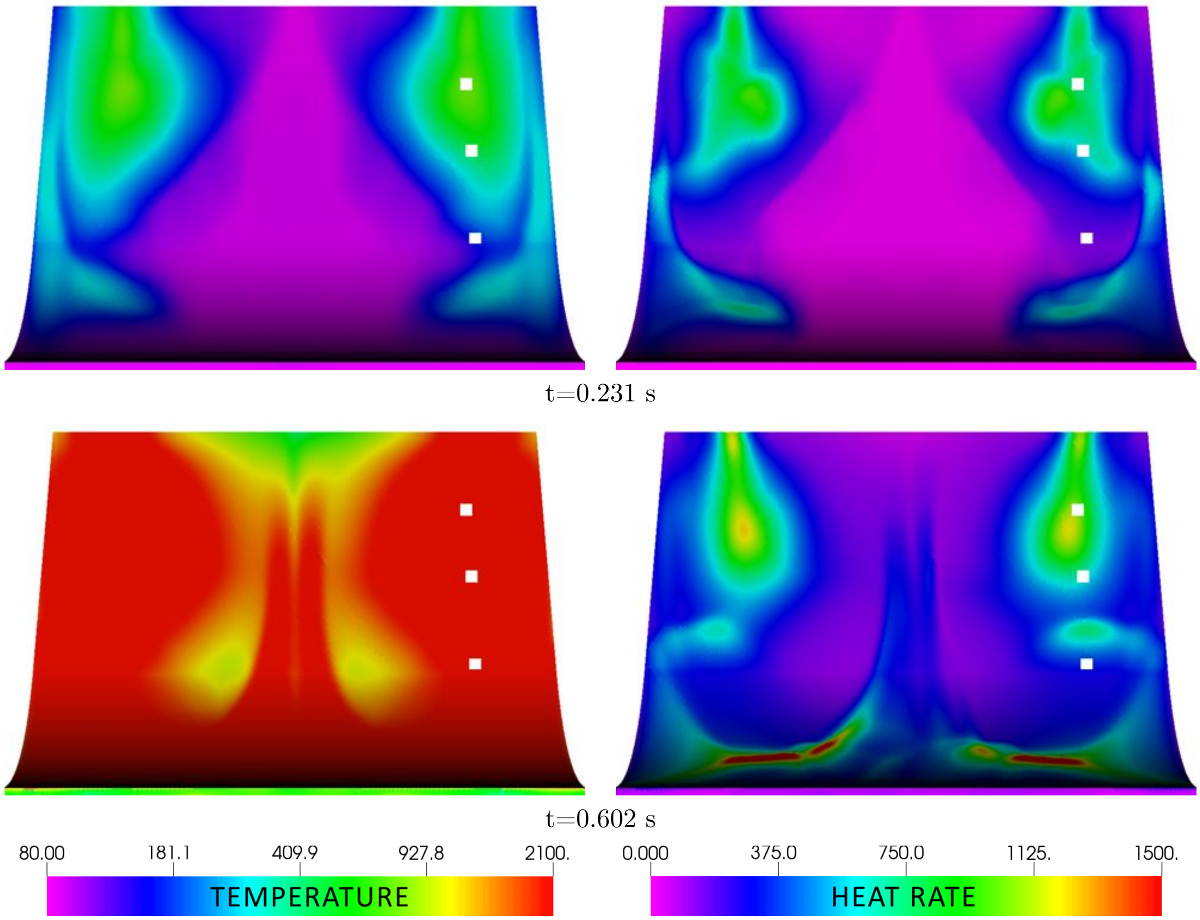

Figure 19: Instantanous temperature distribution (°F) and heat rate (BTU/(ft^{2}s)) at multiple time sequences using LAVA-Unstructured on the north side of the MFD. The sensor locations are superimposed on the surfaces as white squares.

flow field around sensor locations. The upper sensor is located in the high temperature plume impingement location while the middle temperature sensor is on the edge of the region. For the lower sensor, the flow appears to be in the relatively colder spot between the upper and lower impingement locations.

A comparison of the unsteady temperature and heat rate are shown in Figure 20 for the viscous single gas simulation of LAVA-Unstructured and flight medtherm data. The results display the same 0.1 second time delay seen in pressure but shows good agreement otherwise. A large gradient in temperature is visible as the plume impinges on the MFD followed by multiple rises and plateaus. The simulation data reaches the specified melting point temperature limit at a faster rate than the flight data. The discrepancy can be associated with the water sound suppression system reducing surface temperatures. Furthermore, the medtherm sensors are set in stainless steel castings while the numerical simulations place them directly in Fondu Fyre. The lower heat capacitance of the stainless steel contributes to the lower temperature rise. Figure 20b shows a good comparison between the heat rate flight data. A large initial spike in heat rate occurs at the initial impingement and reaches a quasi-steady state value. The flight data show significant spikes in heat rate which can be associated with particle heating.

Similar temperature and heat rate comparisons are shown in Figure 21 for the middle sensor location. The temperature history of the simulation results show a similar trend to the flight data but reach melting temperature at a faster rate. An initial spike is shown followed by multiple small spikes as the flow develops these are evident in both the simulation and flight data. The heat rate also shows a large spike during the initial impingement and reaches a semi-steady value of approximately 300 BTU/(ft^{2}s). The simulation data

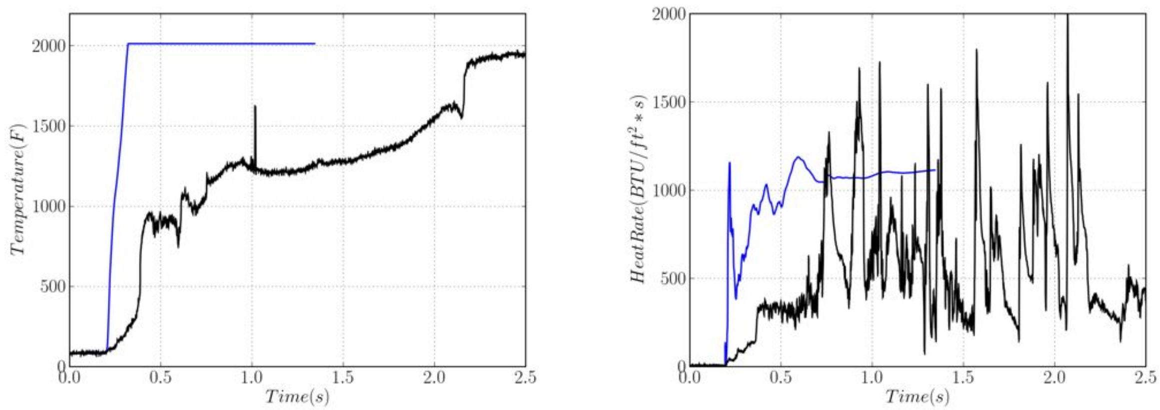

(a) (b)

Figure 20: Unsteady temperature (a) and heat rate (b) history at top sensor location on MFD. Flight data (black –) and LAVA-Unstructured (blue –) are shown.

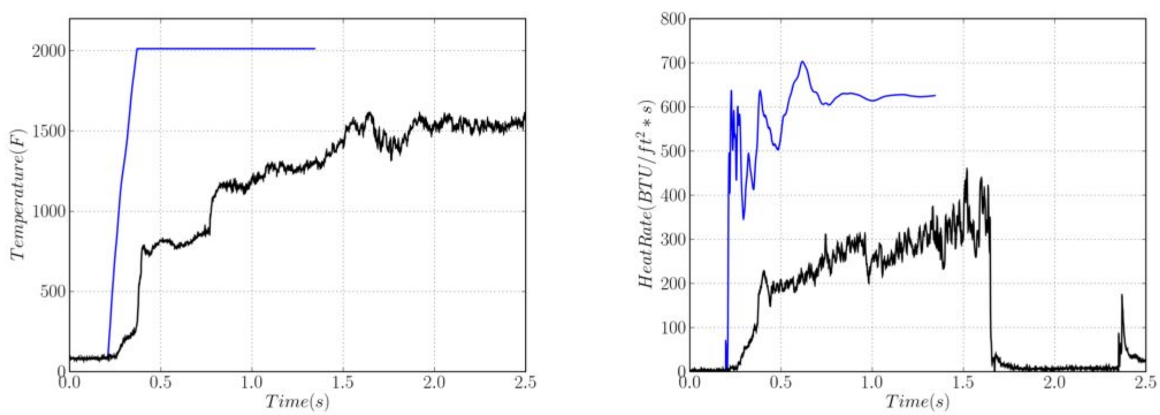

(a) (b)

Figure 21: Unsteady temperature (a) and heat rate (b) history at middle sensor location on MFD. Flight data (black –) and LAVA-Unstructured (blue –) are shown.

shows a similar trend but has a higher mean value. The significant drop in the flight heat rate data at 1.6 seconds is indicative of sensor failure. Figure 22 shows the temperature and heat rate comparison for the bottom sensor. Both the simulation temperature and heat rate are conservative estimates of the flight data results. Overall, results indicate the viscous single gas has similar trends as the flight data.

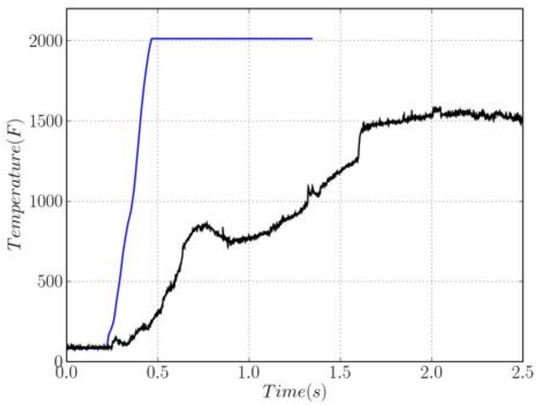

(a)

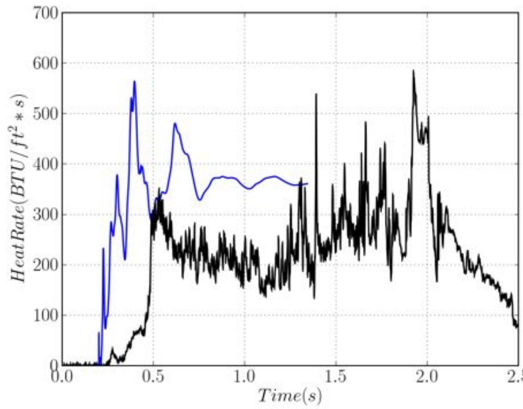

(b)

Figure 22: Unsteady temperature (a) and heat rate (b) history at bottom sensor location on MFD. Flight data (black −) and LAVA-Unstructured (blue −) are shown.

5 Conclusion and Future Work

Progress towards hybrid simulations of the launch environment has been made with the application of LAVA-Cartesian/Unstructured on a 2D trench test case and validation of the individual solvers on a Space Shuttle test case (STS-135). Pressure signatures for the 2D trench case indicated that single gas simulations are adequate while code-to-code comparisons were positive for the hybrid approach in terms of pressure and temperature. The individual flow solvers, LAVA-Cartesian and LAVA-Unstructured, were validated against flight data for the Space Shuttle test case and showed good agreement. The pressure environment was resolved with both LAVA-Cartesian inviscid simulations and LAVA-Unstructured viscous simulations. Pressure amplitudes for the IOP and trends in flight data were captured with both approaches. With the conjugate heat transfer method, temperature and heat rate data from LAVA-Unstructured showed conservative comparisons. Application of the hybrid approach to the Space Shuttle test case is currently underway, as well as a study of the sensitivity of thermal results to material properties. The hybrid grid coupling framework that has been established shows the potential to reduce grid generation time, improve simulation turn-around time and adequately model the launch environment for design analysis.

6 Acknowledgements

This work has been partially been funded by the 21st Century Launch Complex. We would also like to thank Dr. Bruce Vu and Dr. Christopher R. Parlier for providing STS-135 flight data.

References

[1] R. L. Evans and O. L. Sparks. Launch deflector design criteria and their appication to the Saturn C-1 deflector. Technical Note d-1275, NASA, 1963.

[2] C. Kiris, J. Housman, M. Gusman, W. Chan, and D. Kwak. Time-Accurate Computational Analysis of the Flame Trench Applications. In *21st Intl. Conf. on Parallel Computational Fluid Dynamics*, pages 37–41, 2009.

[3] R.H. Nichols and P.G. Buning. User's Manual for OVERFLOW 2.1. Version 2.1t, August 2008.

[4] W. Chan, R.J. Gomez, S. Rogers, and P. Buning. Best Practices in Overset Grid Generation. In *32nd AIAA Fluid Dynamics Conference and Exhibit, St. Louis, Missouri*, Jun 24-26 2002. AIAA–2002–3191.

[5] S. Pandya, W. Chan, and J. Kless. Automation of Structured Overset Mesh Generation for Rocket

Geometries. In *19th AIAA Computational Fluid Dynamics Conference, San Antonio, Texas*, Jun 22–25 2009. AIAA–2009–3993.

[6] M. J. Berger and P. Colella. Local adaptive mesh refinement for shock hydrodynamics. *J. Comput. Phys.*, 82(1):64–84, May 1989.

[7] A. S. Almgren, J. B. Bell, P. Colella, L. H. Howell, and M. L. Welcome. A conservative adaptive projection method for the variable density incompressible Navier-Stokes equations. *J. Comp. Phys.*, 142:1–46, 1998.

[8] M. F. Barad and P. Colella. A Fourth-Order Accurate Local Refinement Method for Poisson's Equation. *J. Comp. Phys.*, 209(1):1–18, October 2005.

[9] M. F. Barad, P. Colella, and S. G. Schladow. An Adaptive Cut-Cell Method for Environmental Fluid Mechanics. *Int. J. Numer. Meth. Fluids*, 60(5):473–514, 2009.

[10] Q. Zhang, H. Johansen, and P. Colella. A fourth-order accurate finite-volume method with structured adaptive mesh refinement for solving the advection-diffusion equation. *SIAM Journal on Scientific Computing*, 34(2):B179–B201, 2012.

[11] P. Colella, D. T. Graves, T. J. Ligocki, D. F. Martin, D. Modiano, D. B. Serafini, and B. Van Straalen. Chombo Software Package for AMR Applications - Design Document. unpublished, 2000.

[12] R. Mittal, H. Dong, M. Bozkurttas, F.M. Najjar, A. Vargas, and A. von Loebbecke. A versatile sharp interface immersed boundary method for incompressible flows with complex boundaries. *Journal of Computational Physics*, 227(10):4825 – 4852, 2008.

[13] S.R. Spalart and S.A. Allmaras. A One-Equation Turbulence Model for Aerodynamic Flows. In *30th Aerospace Sciences Meeting and Exhibit, Reno, NV*, January 1992. AIAA–92–0439.

[14] F.R. Menter. Zonal Two Equation k-ω Turbulence Models For Aerodynamic Flows. In *23rd Fluid Dynamics, Plasmadynamics, and Lasers Conference, Orlando, FL*, July 1993. AIAA–93–2906.

[15] J. Housman, M. Barad, and C. Kiris. Space-time accuracy assessment of cfd simulations for the launch environment. In *29th AIAA Applied Aerodynamics Conference*, June 2011. AIAA-2011-3650.

[16] C. R. Parlier. Pad A main flame deflector sensor data and evaluation. In *2011 Thermal and Fluids Analysis Workshop (TFAWS2011)*, Aug 15–19 2011.

[17] CD-Adapco. Star-ccm+ version 4.02.011 user guide, 2008.

[18] M. L. Norma and K.-H. A. Winkler. Supersonic jets. *Los Alamos Science*, Sping/Summer:38–71, 1985.

[19] C. K. W. Tam, N. N. Pastouchenko, and K. Viswanathan. Fine-scale turbulence noise from hot jets. *AIAA Journal*, 43, 2005.